



HAL
open science

Effective seismic wave velocities and attenuation in partially molten rocks

Vladimir Lyakhovsky, Eyal Shalev, Ittai Kurzon, Wenlu Zhu, Laurent Montesi, Nikolai M Shapiro

► **To cite this version:**

Vladimir Lyakhovsky, Eyal Shalev, Ittai Kurzon, Wenlu Zhu, Laurent Montesi, et al.. Effective seismic wave velocities and attenuation in partially molten rocks. *Earth and Planetary Science Letters*, 2021, 572, pp.117117. 10.1016/j.epsl.2021.117117 . hal-03292087

HAL Id: hal-03292087

<https://hal.science/hal-03292087>

Submitted on 20 Jul 2021

HAL is a multi-disciplinary open access archive for the deposit and dissemination of scientific research documents, whether they are published or not. The documents may come from teaching and research institutions in France or abroad, or from public or private research centers.

L'archive ouverte pluridisciplinaire **HAL**, est destinée au dépôt et à la diffusion de documents scientifiques de niveau recherche, publiés ou non, émanant des établissements d'enseignement et de recherche français ou étrangers, des laboratoires publics ou privés.

1
2 **Effective seismic wave velocities and attenuation in partially molten rocks**
3

4
5 Vladimir Lyakhovsky^{1*}, Eyal Shalev¹, Ittai Kurzon¹, Wenlu Zhu², Laurent Montesi², and
6 Nikolai M. Shapiro^{3,4}
7
8

91. Geological Survey of Israel, Jerusalem, Israel.

102. Department of Geology, University of Maryland, College Park, Maryland, USA

113. Institut de Sciences de la Terre, Université Grenoble Alpes, CNRS (UMR5275), CS 40700,
12 38058 Grenoble Cedex 9, France.

134. Schmidt Institute of Physics of the Earth, Russian Academy of Sciences, Bolshaya
14 Gruzinskaya str., 10-1, 123242 Moscow, Russia
15
16
17

18 *) Corresponding author: vladimir.lyakhovsky@gmail.com
19
20

21 Submitted to EPSL March, 2021

22 Revised June, 2021
23
24
25

26 **Key words:** partial melt, phase transition, wave velocity, attenuation
27
28

29 **Abstract**

30 Significant reduction in mechanical properties, i.e., elastic moduli and seismic wave
31 velocities, as well as enhanced inelastic attenuation is often associated with areas of partially
32 molten rocks. In this paper we suggest a new mechanism responsible for significant reduction of
33 wave velocity and enhanced attenuation. The suggested mechanism considers solid-melt phase
34 transition at thermodynamic equilibrium. Any pressure change, that takes the system out of
35 thermodynamic equilibrium, causes solidification or melting which modifies the heat balance
36 according to the Clausius-Clapeyron equation. The latent heat (sink or source) is transferred away
37 or towards the interface by conductive-advective mechanism heating or cooling the entire rock
38 mass leading to energy loss and dissipation of the mechanical energy and to seismic wave
39 attenuation. We use simplified geometry and derive analytical solutions for wave velocity
40 reduction and attenuation associated with a moving solid-melt interface (Stefan problem). We
41 demonstrate that the latent heat generation due to wave-induced pressure oscillations around
42 thermodynamic equilibrium is an efficient mechanism for energy dissipation and leads to
43 significant reduction in mechanical properties (seismic velocities and attenuation). The highest
44 attenuation occurs when the period of oscillation is close to the heat transfer time scale associated
45 with the size of melt inclusions. The predicted values are approximately in agreement with large
46 scale seismological observations, showing that seismic waves are mostly attenuated within the
47 shallow parts of Earth's crust and mantle, and are associated with possible presence of melt.

48

49 **1. Introduction**

50 Melt fraction is largely present in the crust and uppermost mantle of the Earth. The partially
51 molten rocks are characterized by enhanced mobility because of their elevated buoyancy and
52 reduced viscosity and, therefore, play a key role in many geodynamical processes. Partial melting
53 of silicate rocks occur in regions within the crust and in the uppermost mantle where the solidus-
54 liquidus transition can be reached by different mechanisms such as: decompression (e.g., Niu,
55 1997), heating by uprising hot material such as mantle plumes (e.g., Campbell, 2005),
56 compositional changes such as the addition of water (e.g., Asimow and Langmuir, 2003), or by
57 mechanical processes such as frictional melting (e.g., (Di Toro et al., 2006). The most direct
58 manifestations of the presence of the molten rocks are the volcanic deposits observed at the surface,
59 and the magmatism imprinted in geological records. Initial magmas form at depths and driven by

60 buoyancy, rise toward the surface, through the uppermost mantle and the crust. While volcanic
61 deposits of molten rock reach the surface, most of the magmas and molten rock remain stored at
62 depth. Understanding how the magma and molten rocks are stored at depth is one of the major
63 challenges in volcanology and igneous geology. Traditional views, implying the existence of
64 concentrated “high-melt” volumes, forming well identified intrusions or magma chambers, is
65 challenged today with new concepts suggesting a more distributed storage of melts in a form of
66 low melt-fraction “mush reservoirs” (Jackson et al., 2018). The form of such storage at depth
67 strongly affects the evolution of magmas/melts and their mobility, changing the hydraulic
68 connectivity of volcano-magmatic systems (Pinel et al., 2010). Melt distribution within the shallow
69 layers of the crust is of great importance for estimating the potential volcanic activity. Estimation
70 of the volume of erupted volcanic products from geological records shows that past rates of
71 volcanism were very variable both for individual volcanic systems and for the whole Earth. In
72 particular, the level of volcanic activity that occurred during human history is rather weak
73 compared to some pre-human major events such as explosive super-Plinian eruptions, the
74 emergence of flood basalts and the generation of large igneous provinces (e.g., Bryan et al., 2010);
75 such strong events are often called upon to explain environmental changes and mass extinctions
76 (Sobolev et al., 2011). The possibility of occurrence of new major volcanic episodes with great
77 impact at a global scale cannot be excluded and its understanding requires the estimation of melt
78 distribution within the shallow layers of the crust.

79 The presence of melt is also of major importance for global mantle dynamics and plate
80 tectonics. Mantle convection in the vicinity of the major convergent and divergent plate boundaries
81 is strongly influenced by the melt fraction, present in the subduction zone mantle wedges (e.g.,
82 Gerya and Meilick, 2011) and beneath the mid-oceanic ridges (e.g., Niu, 1997). The partial melt
83 is also suggested to contribute significantly to the mechanical weakness of the asthenosphere (e.g.,
84 Chantel et al., 2016) and to facilitate the widespread small- scale sub-lithospheric convection(e.g.,
85 van Hunen et al., 2005). Partial melt might be present in the continental crust driving fast
86 deformation of the rocks, and affecting the orogenesis (Chen et al., 2018). Also, partial melt can
87 lubricate seismogenic faults (Di Toro et al., 2006) and, therefore, affect earthquake dynamic and
88 seismo-tectonic cycles.

89 Understanding many ongoing key geodynamic processes and related natural hazards
90 requires information on the distribution of partial melt storage systems and reservoirs in the Earth’s

91 crust and upper mantle. This information can be obtained only by methods of deep geophysical
92 sounding, searching for the areas with abnormal physical and mechanical properties. One possible
93 approach is finding the presence of partial melt in the subsurface by searching for elevated
94 electrical conductivity (Watanabe and Kurita, 1993). So far, large scale electromagnetic and
95 magneto-telluric surveys were used to study partially molten rocks located at depths beneath mid
96 oceanic ridges (e.g., Baba et al., 2006) and volcanoes (e.g., Hill et al., 2009).

97 Another approach is to use the significant reduction in mechanical properties, i.e., elastic
98 moduli and seismic wave velocities, as well as enhanced anelastic attenuation in the areas with
99 partially molten rocks that can be measured with different seismological methods (Debayle et al.,
100 2020). This approach is much widely used because of the existence of numerous permanent and
101 temporary seismic networks. In highly active volcanic systems the mobility of melt can lead to
102 recordable seismic radiation (Chouet, 1996; Shapiro et al., 2017). However, in most cases, the
103 detection of molten rocks requires using different methods of seismic imaging. Since it is widely
104 accepted that the shear modulus and S-wave velocity are most affected by the presence of melt (or
105 more generally fluid fraction), the S-wave seismic tomography is particularly suitable to image the
106 regions with presence of significant portions of melt such as in mid-oceanic ridges (e.g., Conder
107 et al., 2002) hotspots (Allen et al., 2002). Strong negative P-wave seismic velocity anomalies can
108 also indicate the presence of melt, especially beneath volcanoes, and in many cases, the V_p/V_s
109 ratio is used to trace the melts (e.g., Koulakov et al., 2020). Melt-induced variations of the elastic
110 moduli also affect the reflectivity structure in the crust and in the uppermost mantle. Therefore,
111 the melt-enriched regions can be imaged with the reflection seismic methods or with its passive
112 seismology analog: the receiver functions (e.g., Rychert et al., 2013). Different methods of
113 attenuation measurement using amplitudes of direct waves (P, S) and the coda of seismograms can
114 be used in different geological settings (e.g., Prudencio and Manga, 2020). The separation of the
115 intrinsic attenuation and scattering is a particularly challenging issue. The latter can be strongly
116 enhanced by the presence of small pockets of partially molten rocks.

117 As mentioned above (Jackson et al., 2018), magma and melt may be stored not within large
118 intrusions or reservoirs but rather distributed over a system of small melt pockets or layers with
119 dimensions smaller than seismic wavelengths. In such cases, the preferred orientation of these
120 small partially molten volumes may result in seismic anisotropy. This mechanism can contribute
121 to the well-known radial seismic anisotropy in the upper mantle (Ekström and Dziewonski, 1998).

122 More recently, radial seismic anisotropy has been discovered beneath some large volcanic systems
123 (e.g., Jaxybulatov et al., 2014) where it is believed to be caused by the presence of large sill
124 complexes, composed of many nearly horizontal layers of magmatic rocks with different degree
125 of partial melting.

126 Interpretation of the seismological observations requires understanding of the effects of the
127 properties of the partially molten rocks on the melt fraction and topology of melt inclusions. Zhu
128 et al. (submitted) approach this problem by numerical simulations of the effective elastic properties
129 of different samples prepared in laboratory from a powder mixture of natural basalt with wide
130 range of melt fraction values. They demonstrate that in spite of complex topology of melt
131 distribution the simple geometrical model of the elastic media with spherical fluid inclusions
132 provides a good approximation for the mechanical behavior of the solid-fluid system. However,
133 their static modelling, similar to most of previous studies, ignores the impact of heat and mass
134 transport across the solid-melt interface associated with pressure oscillations. We utilize the simple
135 geometry of spherical melt inclusions and develop analytical solution predicting the impact of the
136 solid-melt phase transition on the bulk elasticity and wave attenuation.

137 In the next section we briefly review averaging models for effective properties of partially
138 molten rocks. Later we provide key aspects of the existing mechanical models of partially molten
139 rocks. Then we discuss the technique of sample preparation and the applied numerical method.
140 Section 5 describes results of numerical simulations and their comparison with existing models of
141 effective elasticity of partially molten rocks (see Appendix A for model details). Then we
142 summarize the main relations connecting bulk elasticity and wave attenuation with moving
143 boundary between solid and melt phases. The detailed derivations are presented in Appendix B.
144 Our findings lead to practical suggestions that may improve the interpretation of seismological
145 observations in areas with partially molten rocks.

146

147 **2. Effective properties of Partially Molten Rocks**

148 *2.1 Bulk elasticity and seismic wave velocities*

149 A partially molten rock is a composite material with solid and liquid (melt) fractions.
150 Effective elastic properties of composite materials have been studied for decades starting with
151 original works by Voigt (1890) and Reuss (1929) who suggested upper and lower bound values
152 for any given volume fraction of constituents, ignoring the topology of the partially molten rock

153 (see Appendix A for detailed description of these and other models). The Voigt (1890) iso-strain
154 model assumes that all constituents have the same strain and provides the upper bound value, while
155 the Reuss (1929) iso-stress assumption leads to the lower bound value. In the case of the solid-
156 melt system with zero shear modulus of the liquid phase, lower bound value for the shear modulus
157 is zero. Converting elastic moduli to V_p and V_s values allows estimating their expected reduction
158 as a function of the melt fraction (Fig. 1). The expected reduction of the V_p values is relatively
159 minor, smaller than 20% velocity reduction for melt fractions of up to 25% (blue curves in Fig. 1).
160 However, the possible range of V_s values is large (red curves in Fig. 1). The iso-strain, Voigt model
161 predicts only minor reduction, whereas the iso-stress model predicts zero V_s values. This wide
162 range is not useful for practical applications and cannot be used to constrain the melt fraction.
163 More realistic bounds giving the narrowest possible range of bulk elasticity without specifying the
164 geometries of the melt inclusions is the Hashin–Shtrikman–Walpole models. Several models
165 consider sphere or ellipsoid inclusion shape and developed analytical solutions (equations a3-a5,
166 Appendix A) connecting effective elastic properties with melt fraction. Several numerical methods
167 such as self-consistent and differential effective medium methods were proposed to account for
168 inclusion interaction and wide range of possible geometries. These methods as well as more
169 accurate evaluation of the effective elastic properties achieved by characterization of the
170 microstructure geometry are briefly discussed in the Appendix A.

171

172 *2.2 Wave attenuation*

173 Quantitative interpretation of seismic wave attenuation in partially molten rocks addresses
174 two general mechanisms. One mechanism considers viscous dissipation due to melt flow or squirt
175 flow in thin films (e.g., Mavko et al., 2009; O’Connell and Budiansky, 1977). Another mechanism
176 addresses dislocation-diffusion stress relaxation in distributed melt pockets or inclusions (e.g.,
177 Karato and Spetzler, 1990; Morris and Jackson, 2009). Both approaches were examined in
178 theoretical and laboratory studies, using natural rocks and synthetic materials, quantifying the
179 seismic attenuation, and trying to establish a physical understanding of these mechanisms (Faul
180 and Jackson, 2015)(Yamauchi and Takei, 2016). Each approach has its shortcomings; while
181 viscous dissipation, due to melt flow, requires unrealistically high melt viscosity (Faul and
182 Jackson, 2015), the dislocation-diffusion mechanism does not explain the strong association of
183 attenuation with the onset of melting (Fontaine et al., 2005).

184 The relaxation time for a melt-squirt within elliptical inclusions was derived by (O’Connell
185 and Budiansky, 1977). In the case when fluid fills narrow crack-like zones, the scaling relations
186 should account for the crack aspect ratio or the ratio between opening and length (c/a). They
187 concluded that the most efficient attenuation of fluid-saturated cracked solids is expected for a
188 frequency range defined by two bounding frequencies:

$$189 \quad \omega_1 = \frac{K}{\eta} \left(\frac{c}{a} \right)^3 \quad \text{and} \quad \omega_2 = \frac{\mu}{\eta} \left(\frac{c}{a} \right) \quad (1)$$

190 This frequency range, as well as the general time scale for the transient deformation, is associated
191 with the stress relaxation process characterized by the Maxwell relaxation time defined as the ratio
192 between fluid viscosity and elastic modulus of the rock mass. Viscosity of dacites and rhyolitic
193 melts, that are expected to be present in the magmatic systems of the continental crust, is relatively
194 high. The viscosity of rhyolite may be as high as 10^{11} Pa s for dry melts and decrease to about 10^6
195 Pa s depending on water content. The Maxwell relaxation time for these melts is of the order of
196 10^{-3} - 10^{+2} s, overlapping the seismological frequency range. Therefore the (O’Connell and
197 Budiansky, 1977) analysis of fluid-filled cracks could well encompass the seismological
198 observations. However, for typical viscosity range of basaltic melts 10^0 - 10^2 Pa s and elastic
199 modulus of the order of tens GPa, the Maxwell relaxation time is of the order of 10^{-7} - 10^{-9} s, and
200 the effects associated with visco-elastic relaxation are negligibly small after very short time
201 intervals. Accordingly, we may expect significant attenuation only at very high frequency waves.
202 More accurate estimation (eq. 1) predicts that even for a small aspect ratio $c/a \sim 10^{-2}$, the typical
203 frequency range is above 1 KHz, which is well above the seismological frequency range. This was
204 already noted by (Mavko, 1980; Mavko et al., 2009), who also discussed squirt flow mechanism.

205 These estimations are compatible with results discussed by Faul et al. (2004) who noted
206 that experimentally observed attenuation in melt-bearing olivine polycrystals reported by Jackson
207 et al. (2004) is not compatible with melt squirt flow through an observed small pipe with aspect
208 ratios around $c/a \sim 10^{-1}$. They also noted that this flow mechanism requires unrealistically high
209 melt viscosity ($\sim 10^4$ Pa s). Faul et al. (2004) suggested an alternative stress relaxation mechanism
210 introducing effective viscosity for olivine-olivine grain boundary regions. Adjusting high “grain-
211 boundary viscosities” ($\sim 10^6$ Pa s) allow fitting the observed attenuation; however, the background
212 physical mechanism, responsible for temperature-dependent attenuation, is still not clear.

213 In addition, most of the recent works discuss different mechanisms for shear attenuation
214 and neglect bulk attenuation. Vaišnys (1968) and Mavko (1980) discussed the mechanism of bulk
215 attenuation and noted the role of the phase transition between solid and melt phases due to wave-
216 induced pressure oscillations. Li and Weidner (2008) reported results of a complicated laboratory
217 measurement demonstrating effects associated with the presence of phase changes. Their results
218 support the velocity decrease and bulk attenuation observed during loading with a period of 1,000
219 s and the softening observed at low amplitudes and shorter periods. Ricard et al. (2009) and Durand
220 et al. (2012) investigated seismic wave attenuation due solid-solid phase transformation. They
221 considered finite rate of kinetics, but without latent heat generation. Their model successfully
222 predicted seismic mode attenuation associated with phase transition at 410 km depth (Durand et
223 al., 2012). However, this attenuation mechanism is not very efficient for body waves with typical
224 frequency range 0.1 – 1 Hz. In the case of the solid-melt phase transition, the characteristic time
225 scale of the of the heat transport generated at the solid-melt interface (latent heat) varies between
226 milliseconds to tens of seconds for melt inclusions of the sizes ranging from tens microns to
227 centimeter scale (Mavko, 1980). Because latent heat is very efficient in releasing energy, it may
228 cause significant attenuation. In this study we develop the analytical solution predicting the impact
229 of the heat generated at the solid-melt phase transition on the bulk elasticity and wave attenuation,
230 considering infinitely fast kinetics.

231

232 **3. Method**

233 *3.1 Bulk elasticity, no mass/heat transfer.*

234 Zhu et al. (2011) obtained high-resolution 3-D determinations of melt distribution in
235 experimentally produced olivine-basalt aggregates using X-ray synchrotron microtomography.
236 Olivine-basalt aggregates with melt fractions of 0.02, 0.05, 0.10, and 0.20 were synthesized from
237 powder mixtures of pulverized natural forsterite and MORB. The spatial resolution of the
238 synchrotron microtomographic images is ~0.7 microns. Comparison to the conventional 2-D
239 scanning electron microscopy (SEM) images of the same samples demonstrated that the
240 microtomographic method captured realistic melt distribution in 3-D over a large representative
241 volume (Zhu et al., 2011). More information regarding the experimental charges and the image
242 analysis could be found in (Miller et al., 2014).

243 Using the reported 3-D melt geometries, Zhu et al. (submitted) recently conducted finite
244 element deformation experiments to obtain the effective bulk and shear moduli of these
245 experimental charges. In the numerical simulations, the numerical elements were dictated by the
246 pixel size of the tomography image with every pixel represented by a cubic brick separated into
247 five tetrahedron elements. The grid avoids any smoothing or averaging of the observed
248 microstructure. The material properties of each pixel (set of five tetrahedron elements) are defined
249 as solid or melt according to the tomographic image. Following (Hammond and Humphreys,
250 2000), we use $K_S = 124$ GPa, $K_M = 64$ GPa, and $\mu_S = 40$ GPa (solid Poisson ratio is 0.28). Infinite
251 viscosity (zero fluidity) is defined for the solid phase, while typical viscosity of 10 Pa s and zero
252 shear modulus are adopted for the melt phase. The viscous strain component act to dampen
253 deformation and facilitates the numerical transient phase that goes from the initial un-deformed
254 equilibrium state to the final static deformed equilibrium one. Boundary conditions for every
255 model run are set according to the simulated loading, i.e., 3-D compaction or uniaxial load. Static
256 stress distribution is simulated using our 3-D code utilizing Fast Lagrangian Algorithm verified in
257 many previous studies.

258 The actual melt fraction, calculated for every sub-volume, depends on the amount of melt
259 generated in the original laboratory sample and also varies between different sub-volumes of the
260 same sample representing the heterogeneity and complex topology of the melt distribution. The
261 lack of any clustering or any preferred location of markers in Fig. 2 corresponding to the size of
262 the numerical grid (100, 200, 300, and 400 pixels) confirms that the obtained results are robust and
263 there is no meaningful grid dependency. Colored lines in Fig. 2 show effective elastic moduli
264 predicted by different analytical models discussed in Appendix A. Results of numerical
265 simulations of the effective elastic properties demonstrate that the simple geometrical model of the
266 elastic media with spherical melt inclusions provide the most reliable approximation for the
267 mechanical behavior of the solid-fluid system, in spite of very simplified topology. This topology
268 of the melt distribution in a form of spherical inclusion located in the center of equal cells
269 (schematically shown in Fig. 3) predicts surprisingly well the elastic properties of partially molten
270 rocks, and will be used in the next section to study impact of heat and mass transport across the
271 solid-melt interface.

272

273 *3.2 Analytical solution of solid-melt phase transition, bulk elasticity and wave attenuation.*

274 A small wave-induced pressure change at a solid-melt interface disturbs the
275 thermodynamic equilibrium and leads to certain motion of the interface. We develop a model for
276 cyclic load with a given amplitude and frequency keeping in mind effects associated with
277 propagation of monochromatic waves. Transient effects related to a final duration of the wave
278 package and temporal variations of the oscillation amplitudes are not considered here. Pressure
279 and deviatoric stress in the solid phase and pressure in the melt, are coupled by stress continuity at
280 the solid-melt interface during external wave-induced load and fluid pressure oscillations. For
281 typical wave amplitude 10^{-5} – 10^{-7} m and wavelength between 0.5–5 km, the deformations of about
282 10^{-8} – 10^{-10} disturbs the thermodynamic equilibrium. Mathematical formulation of this moving
283 boundary or Stefan problem includes heat, mass, and force balance equations. Any pressure change
284 takes the system out of the thermodynamic equilibrium and causes solidification or melting which
285 change the heat balance according to the Clausius-Clapeyron equation. The latent heat (sink or
286 source) is transferred away or towards the interface by conductive-advective mechanism
287 heating/cooling the entire rock mass leading to the energy loss and dissipation of the mechanical
288 energy or seismic wave attenuation. An analytical solution is derived for stress distribution and
289 heat exchange between melt inclusion and solid shell. We neglect the spatial temperature
290 distribution in small melt inclusion. In larger inclusions, effective mixing of the low viscosity fluid
291 probably eliminates any temperature gradients. Therefore we solve for the heat transport only in
292 the solid phase. The analytical solution for the heat balance equation, including latent heat
293 associated with the motion of the solid-melt interface, as well as temperature variations of the melt
294 inclusion, gives the relation between pressure and volumetric strain oscillations. Finally, the
295 derived compressibility of the rock and melt assemblage depends on the characteristics of the
296 external wave-induced forcing. Wave attenuation, or quality factor (Q) is calculated from the time
297 delay between pressure and strain oscillations, or the ratio between real and imaginary bulk
298 moduli.

299

300 **5. Results**

301 *Solid-melt phase transition, bulk elasticity and wave attenuation.*

302 Numerical model simulating the effective elastic properties and results presented in Fig. 2
303 are obtained assuming mass conservation of melt and solid phases without any mass exchange
304 associated with solid-melt phase transition. However, even small wave-induced pressure change

305 at a solid-melt interface disturbs the thermodynamic equilibrium and leads to certain motion of the
 306 interface. Pressure changes move the system out of thermodynamic equilibrium, causing
 307 solidification or melting which change the heat balance according to the Clausius-Clapeyron
 308 equation. The latent heat (sink or source) is transferred away or towards the interface by
 309 conductive-advective mechanism, heating or cooling the entire rock mass, leading to energy loss
 310 and dissipation of the mechanical energy and to seismic wave attenuation. The presented model is
 311 based on the simplified cell geometry representing the partially molten rock as a set of equal elastic
 312 cells with spherical melt inclusions (Fig. 3). The simplified cell geometry allows deriving
 313 analytical relations for stress distribution and heat exchange between melt inclusion and solid shell
 314 considering three different regimes. Each cell representing the solid-melt system is at initial
 315 pressure and temperature (P_0, T_0), corresponding to the thermodynamic equilibrium according to
 316 the phase diagram. The propagating pressure wave, with frequency ω and long wavelength (well
 317 above the cell size) may be considered as time-dependent pressure perturbations at the outer cell
 318 boundary, $P_S(t) = \delta P_S e^{i\omega t}$ (Fig. 3). The elastically deformed solid part of the cell transforms this
 319 pressure to the melt inclusion with a certain pressure factor ψ , i.e., melt pressure changes
 320 proportionally to the pressure wave amplitude, $\delta P_M e^{i\omega t} = \psi \cdot \delta P_S e^{i\omega t}$, (see Appendix B for
 321 complete mathematical derivations). This pressure change violates the thermodynamic
 322 equilibrium, which is re-established by the motion of the solid-melt interface. According to the
 323 slope of the phase diagram (Clausius-Clapeyron slope, α) the temperature changes proportionally
 324 to the pressure, which relates the latent heat (heat of phase transformation) to the rate of pressure
 325 change with temperature (see table 1 for notations):

$$\frac{dP}{dT} = \frac{L \cdot \rho^2}{T \cdot \Delta\rho} = \alpha \quad (2)$$

327 Neglecting the time required to re-establish the thermodynamic equilibrium, the temperature
 328 variations at the solid-melt interface are:

$$T_M(t) - T_0 = \psi \delta P_S e^{i\omega t} / \alpha \quad (3)$$

330 Heat balance associated with moving solid-melt interface includes latent heat and heating/cooling
 331 of the melt inclusion and surrounding solid. Heat variation of small melt inclusion is proportional
 332 to its mass and temperature variation, while heat flux in the solid part of the cell is proportional to
 333 the temperature gradient at the interface. In Appendix B we provide exact solution for the

334 temperature distribution in the solid shell with the oscillating boundary condition (3). The obtained
 335 solution, in the form of

$$336 \quad T(r, t) = \frac{A}{r} e^{ikr} e^{i\omega t} \quad (4)$$

337 allows calculating the diffusive heat flux towards the solid shell surrounding the melt inclusion:

$$338 \quad dH = 4\pi\kappa\psi \frac{\delta P_S}{\alpha} R e^{i\omega t} (A_1 + iA_2) dt \quad (5)$$

339 where

$$340 \quad A_1 = 1 + \sqrt{\frac{\omega R^2}{2D}} - \left[\cos\left(\sqrt{\frac{\omega}{2D}} (2S - R)\right) \left(1 + \sqrt{\frac{2\omega S^2}{D}}\right) + \sin\left(\sqrt{\frac{\omega}{2D}} (2S - R)\right) \sqrt{\frac{2\omega S^2}{D}} \right] e^{-\sqrt{\frac{\omega}{2D}} (2S - R)}$$

341 (6)

$$342 \quad A_2 = \sqrt{\frac{\omega R^2}{2D}} + \left[\sin\left(\sqrt{\frac{\omega}{2D}} (2S - R)\right) \left(1 + \sqrt{\frac{2\omega S^2}{D}}\right) - \cos\left(\sqrt{\frac{\omega}{2D}} (2S - R)\right) \sqrt{\frac{2\omega S^2}{D}} \right] e^{-\sqrt{\frac{\omega}{2D}} (2S - R)}$$

343 Solving the heat balance equation, which also includes latent heat associated with the motion of
 344 the solid-melt interface, as well as temperature variations of the melt inclusion, gives the relation
 345 between pressure and volumetric strain oscillations. Their ratio ($K = K_R + iK_I = -\delta P_S / \delta \varepsilon_V$) is
 346 the complex bulk modulus:

$$347 \quad K = \left\{ \frac{1}{K_e} + \frac{\beta\gamma\psi}{\alpha L \rho_S} \left[\rho_M C_P + (A_2 - iA_1) \frac{3\kappa}{\omega R^2} \right] \right\}^{-1} \quad (7)$$

348 The ratio K_R/K_I between the real and imaginary parts of the bulk modulus (7) defines the bulk
 349 quality factor, Q , of the media (see Appendix B)

$$350 \quad Q = \frac{\alpha L \rho_S \omega R^2 + \beta\gamma\psi K_e \rho_M C_P \omega R^2 + \beta\gamma\psi K_e A_2 3\kappa}{K_e \beta\gamma\psi A_1 3\kappa} \quad (8)$$

351 These derivations demonstrate that moving solid-melt phase boundary due to wave-
 352 induced pressure oscillations leads to additional reduction of the bulk modulus, K_e , estimated from
 353 the elastic deformation and provides efficient mechanism for wave attenuation. Most of the
 354 material properties in (6, 7, 8) are well defined with relatively small uncertainty range (e.g., Ricard,
 355 2015). The exception is the product of the Clausius-Clapeyron slope and latent heat values, which
 356 according to (2) is expressed as:

$$357 \quad \alpha L = \frac{\alpha^2 T \Delta \rho}{\rho^2} \quad (9)$$

358 Therefore, we ignore the uncertainty in most of the parameters presented in Table 1, and study the
 359 sensitivity of the model predictions to the reasonable variations of the Clausius-Clapeyron slope
 360 values $\alpha = 3, 6, 9$ MPa/ $^\circ$ K (Bina and Helffrich, 1994). Larger slope values, from ~ 7.5 MPa/ $^\circ$ K at

361 low pressures up to ~ 30 MPa/ $^{\circ}$ K at 10 GPa were reported by (Hirschmann, 2000) for various
362 compositions of mantle Peridotites.

363 Fig. 4 shows reduction of the bulk modulus as a function of the melt fraction calculated
364 using eq. 7. We define the cell-size, as the typical distance between melt pockets. In brittle
365 rheology, these melt pockets are typically grain-size away from each other, while for ductile
366 rheology they would be further separated. For small cell-size (Fig. 4a for $S_0=0.5$ mm) the reduction
367 is larger than for relatively large cell-size (Fig. 4b for $S_0=5.0$ mm). In both cases smaller Clausius-
368 Clapeyron slope values lead to more significant effect, since the amplitude of the temperature
369 oscillations at the solid-melt interface (3) is proportional to $1/\alpha$. The most pronounced change
370 above 80% reduction occurs at low melt fraction values below 2% for $\alpha = 3$ and 6 MPa/ $^{\circ}$ K (Fig.
371 4a) and then remains about constant. Larger cell-size (Fig. 4b) causes gradual reduction of the bulk
372 modulus. Values of the quality factor (Q) for 1 Hz p-wave frequency, calculated using eq. 8, also
373 strongly depend on these factors (Fig. 5). For small grain size ($S_0=0.5$ mm) the reduction is
374 practically abrupt at very low melt fraction values and then Q remains practically constant within
375 the values shown by the red polygon in Fig. 5. For larger $S_0=5.0$ mm, the Q decrease is steeper for
376 small α -values and approach about constant value at melt fraction values above $\sim 5\%$. Since the
377 presented model ignores wave attenuation in the solid phase, the Q-values go to infinity for zero
378 melt fraction value ($\beta=0$).

379 Wave attenuation predicted by the model, is strongly frequency-dependent (Fig. 6). Less
380 attenuation or higher Q-values are obtained at very low and high frequency values. If the oscillation
381 period is very large, the whole cell volume is heated to the equilibrium temperature and the delay
382 associated with heat transfer is small. Similarly, heat transfer can be neglected at very small period
383 values. The highest attenuation occurs when the period of oscillation is close to the heat transfer
384 time scale. In this condition, any heating that occurs due to Solid-melt phase transition during the
385 oscillation is affecting the entire cell and therefore causing high attenuation. The time needed to
386 transfer heat over the cell size or the characteristic time scale of conductive heat transfer over the
387 cell size is defined as S_0^2/D . Therefore, the largest attenuation occurs when $f \cdot S_0^2/D \sim 1$. For small
388 cell-size (Fig. 6a) maximum attenuation is expected at frequency range, f , between 1 and 10 Hz.
389 Q-values are very low and weakly depend on the melt fraction. One order of magnitude increase
390 in the cell-size causes two orders of magnitude (S_0^2) frequency change (0.01 - 0.1 Hz) for maximum

391 attenuation (Fig. 6b). In both cases, the increase in Q-values at low frequencies only weakly
392 depends on the melt fraction, while it is significantly more sensitive at high frequencies.

393

394 **6. Discussion**

395 Understanding how magma or molten rocks are stored at depth is one of the major
396 challenges in volcanology, igneous geology, mantle dynamics, and plate tectonics. Many of the
397 ongoing geodynamic key processes and related natural hazards require information on the
398 distribution of partial melt storage system and reservoirs in the Earth's crust and upper mantle.
399 Seismological methods are often used to show areas of significant reduction in seismic wave
400 velocities and enhanced wave attenuation, and are interpreted as revealing pockets of partially
401 molten rocks. Interpretation of the seismological observations requires understanding of the effects
402 of the properties of the partially molten rocks on the melt fraction and on the topology of melt
403 inclusions.

404 Previous studies show that viscous dissipation due to flow or squirt of the melt with realistic
405 viscosity range is small and expected attenuation is well below the typical values for the partially
406 molten rocks. The developed analytical model shows that phase transition is an efficient
407 mechanism for strong attenuation and for the reduction of wave velocity. The model adopts cell
408 geometry for spherical melt inclusions in partially melted rocks (Fig. 3). Previous results discussed
409 by Zhu et al. (submitted) and shown in Fig. 2 demonstrate that in spite of a complex melt topology,
410 this simple geometrical model provides surprisingly good approximation for the effective rock
411 elasticity. This important result allows using analytical solutions, assuming spherical inclusions,
412 for estimating effective elastic properties and modeling wave attenuation.

413 The most realistic bounds giving the narrowest possible range of bulk elasticity leaving
414 solid-melt phase transition out of the consideration is the Hashin–Shtrikman–Walpole model.
415 Their model predicts relatively minor reduction in both pressure and shear wave velocities with
416 melt fraction (Fig. 7). However, even for relatively large cell-size ($S_0=5$ mm) and intermediate
417 Clausius-Clapeyron slope value, $\alpha = 5$ MPa/ $^{\circ}$ K, the reduction in the bulk modulus associated with
418 the phase transition is dominant (Fig. 7). The analytical solution considers only spherical symmetry
419 and volumetric deformation, and formally cannot relate phase transition to shearing, which in
420 perfect material is decoupled from volumetric deformation. However, original studies by Reynolds
421 (1885) and Skempton (1954), have shown that shear stress is strongly coupled with pressure, and

422 therefore the formal decoupling is in doubt. Taking into account the relation between S-wave
423 induced shearing and pressure, we speculate here that propagating S-waves will also lead to similar
424 phase boundary motion, i.e., velocity reduction and attenuation. Dashed red line in Fig. 7 shows
425 the inferred shear modulus reduction using the same factor as for the P-waves. More accurate
426 relations for the S-waves will be examined in future study.

427 In summary, the analyzed mechanism of reduction in mechanical properties associated
428 with the phase transition predicts that the presence of significant amount of melt in the rocks would
429 result in a strong decrease in seismic wave velocities associated with a strong increase of their
430 attenuation. Preliminary consideration also indicates that the velocity decrease should be more
431 enhanced for S wave (Fig. 7), resulting in the increase of the V_p/V_s ratio. This implies that
432 simultaneous measurement of these properties could help to better constrain the melt content in
433 studied geological objects such as, for example, volcanic systems. A key parameter for
434 interpretation of such results is the average cell-size S_0 , that remains poorly known. Results shown
435 in Fig. 6 indicate that this parameter cannot be too small ($< 1\text{mm}$) because in this case the waves
436 at frequencies between 1 and 10 Hz (i.e. typical range of observation for volcanic earthquakes)
437 would be completely dissipated ($Q < 5$). Considering the millimeter or centimeter scale of the melt
438 distribution spatial heterogeneity would result in more appropriate predictions with Q varying
439 between 10 and several hundreds at 1 Hz. Moreover, with such values of S_0 , the model predicts an
440 approximately power-law increase of Q at high frequencies, i.e., the behavior reported from field
441 observations and laboratory experiments (Lekić et al., 2009). Overall, the predicted values are
442 approximately in agreement with large scale seismological observations showing that seismic
443 waves are mostly attenuated within the shallow parts of the Earth's crust and mantle, and
444 associated with possible presence of melt, such as in mid-oceanic ridges and island arcs or beneath
445 large volcanic systems. The model is also in agreement with observed significant correlation
446 between the regional-scale tectonics and the geographical distributions of uppermost-mantle
447 velocities and attenuation for S and P waves. So far, average Q being as low as ~ 60 in the upper
448 mantle low velocity zone, where significant amount of melt may be expected (e.g., Thybo, 2006).

449 The presented model considers latent heat generation at the solid-melt phase transition and
450 heat transport near the interface. Adopting infinitely fast kinetics, the model predicts the realistic
451 body wave attenuation with the frequency range 0.1-1 Hz. The alternative approach considering
452 solid-solid transition with finite phase (Durand et al., 2012; Ricard et al., 2009), predicts maximum

453 attenuation at significantly lower frequency range typical for free oscillations. The real case might
454 be somewhat in between and the complete model should consider both type of the phase
455 transitions.

456

457 **7. Conclusion**

458 In spite of the complex structure of partially molten rocks, effective elastic moduli can be
459 approximated assuming spherical melt inclusions geometry, which implies that the exact topology
460 of the melt even at high melt fraction values is not crucial. Viscous flow mechanisms for basaltic
461 melts can cause attenuation only at very high frequency waves. Explaining observed wave
462 attenuation in partially molten peridotite rocks using viscous flow requires adjusting unrealistically
463 high viscosities.

464 We present a new mechanism for wave velocity reduction and attenuation associated with
465 moving solid-melt interface (Stefan problem), and latent heat generation due to wave-induced
466 pressure oscillations around thermodynamic equilibrium. The reduction in mechanical properties
467 (seismic velocities) associated with the phase transition is shown to be significant. The highest
468 attenuation occurs when the period of oscillation is close to the heat transfer time scale. In this
469 condition, any heating that occurs due to Solid-melt phase transition during the oscillation is
470 affecting the entire cell and therefore causes high attenuation.

471

472 **Acknowledgements**

473 We thank Claude Jaupart and Navot Murag for discussions. The paper benefited from useful
474 comments by two anonymous referees and the editor, Hans Thybo. This study was supported by
475 the Russian Ministry of Education and Science (Grant 14.W03.31.0033) and by the European
476 Research Council under the European Union Horizon 2020 research and innovation program
477 (Grant Agreement 787399-SEISMAZE).

478

479 Table 1. Values of the model constants.

Notation	Parameter	Value/units
K_S	Solid bulk modulus	124 GPa
μ_S	Solid shear modulus	64 GPa
ν_S	Solid Poisson ratio	0.28
K_M	Melt bulk modulus	40 GPa
K_e	Effective bulk modulus	GPa
μ_e	Effective shear modulus	GPa
β	Melt fraction	0-20%
α	Clausius-Clapeyron slope	1-10 MPa/°K
κ	Heat conductivity	3.5 J/s m °K
C_p	Heat capacity	1 kJ/kg °K
L	Specific latent heat	10^2 - 10^3 kJ/kg
ρ_S	Solid density	3,500 kg/m ³
ρ_M	Melt density	3,000 kg/m ³
$D = \frac{\kappa}{\rho_S C_P}$	Thermal diffusivity	$1 \cdot 10^{-6}$ m ² /s
S_0	Cell radius	0.5 - $5 \cdot 10^{-3}$ m
$R = S_0 \sqrt[3]{\beta}$	Inclusion radius	M
γ	Volumetric strain factor	0.25
ψ	Pressure factor	0.54

480

481 **8. References**

- 482 Allen, R.M., Nolet, G., Morgan, .W.J., Vogfjörd, K., Bergsson, B.H., Erlendsson, P., Foulger,
483 G.R., Jakobsdóttir, S., Julian, B.R., Pritchard, M., 2002. Imaging the mantle beneath Iceland
484 using integrated seismological techniques. *J. Geophys. Res. Solid Earth* 107, ESE-3.
485 Asimow, P.D., Langmuir, C.H., 2003. The importance of water to oceanic mantle melting
486 regimes. *Nature* 421, 815–820.
- 487 Baba, K., Chave, A.D., Evans, R.L., Hirth, G., Mackie, R., 2006. Mantle dynamics beneath the
488 East Pacific Rise at 17 S: Insights from the Mantle Electromagnetic and Tomography
489 (MELT) experiment. *J. Geophys. Res. Solid Earth* 111.
- 490 Bina, C.R., Helffrich, G., 1994. Phase transition Clapeyron slopes and transition zone seismic
491 discontinuity topography. *J. Geophys. Res. Solid Earth* 99, 15853–15860.
- 492 Bryan, S.E., Peate, I.U., Peate, D.W., Self, S., Jerram, D.A., Mawby, M.R., Marsh, J.S.G.,
493 Miller, J.A., 2010. The largest volcanic eruptions on Earth. *Earth-Science Rev.* 102, 207–
494 229.
- 495 Campbell, I., 2005. Large Igneous Provinces and the Mantle Plume Hypothesis. *Elements* 1,
496 265–269.
- 497 Chantel, J., Manthilake, G., Andraut, D., Novella, D., Yu, T., Wang, Y., 2016. Experimental
498 evidence supports mantle partial melting in the asthenosphere. *Sci. Adv.* 2, e1600246.
- 499 Chen, J., Gaillard, F., Villaros, A., Yang, X., Laumonier, M., Jolivet, L., Unsworth, M., Hashim,
500 L., Scaillet, B., Richard, G., 2018. Melting conditions in the modern Tibetan crust since the
501 Miocene. *Nat. Commun.* 9, 1–13.
- 502 Chouet, B., 1996. Long-period volcano seismicity: its source and use in eruption forecasting.
503 *Nature* 380, 309–316.
- 504 Conder, J.A., Forsyth, D.W., Parmentier, E.M., 2002. Asthenospheric flow and asymmetry of the
505 East Pacific Rise, MELT area. *J. Geophys. Res. Solid Earth* 107, ETG-8.
- 506 Debayle, E., Bodin, T., Durand, S., Ricard, Y., 2020. Seismic evidence for partial melt below
507 tectonic plates. *Nature* 586, 555–559.
- 508 Di Toro, G., Hirose, T., Nielsen, S., Pennacchioni, G., Shimamoto, T., 2006. Natural and
509 experimental evidence of melt lubrication of faults during earthquakes. *Science* (80-.). 311,
510 647–649.
- 511 Durand, S., Chambat, F., Matas, J., Ricard, Y., 2012. Constraining the kinetics of mantle phase
512 changes with seismic data. *Geophys. J. Int.* 189, 1557–1564.
- 513 Ekström, G., Dziewonski, A.M., 1998. The unique anisotropy of the Pacific upper mantle.
514 *Nature* 394, 168–172.
- 515 Faul, U., Jackson, I., 2015. Transient Creep and Strain Energy Dissipation: An Experimental
516 Perspective. *Annu. Rev. Earth Planet. Sci.* [https://doi.org/10.1146/annurev-earth-060313-
517 054732](https://doi.org/10.1146/annurev-earth-060313-054732)
- 518 Faul, U.H., Fitz, G.J.D., Jackson, I., 2004. Shear wave attenuation and dispersion in melt-
519 bearing olivine polycrystals: 2. Microstructural interpretation and seismological
520 implications. *J. Geophys. Res. Solid Earth* 109.
- 521 Fontaine, F.R., Ildefonse, B., Bagdassarov, N.S., 2005. Temperature dependence of shear wave
522 attenuation in partially molten gabbro-norite at seismic frequencies. *Geophys. J. Int.* 163,
523 1025–1038. <https://doi.org/10.1111/j.1365-246X.2005.02767.x>
- 524 Gerya, T., Meilick, F.I., 2011. Geodynamic regimes of subduction under an active margin:
525 effects of rheological weakening by fluids and melts. *J. Metamorph. Geol.* 29, 7–31.
- 526 Hammond, W.C., Humphreys, E.D., 2000. Upper mantle seismic wave velocity: Effects of

527 realistic partial melt geometries. *J. Geophys. Res. Solid Earth* 105, 10975–10986.
 528 Hill, G.J., Caldwell, T.G., Heise, W., Chertkoff, D.G., Bibby, H.M., Burgess, M.K., Cull, J.P.,
 529 Cas, R.A.F., 2009. Distribution of melt beneath Mount St Helens and Mount Adams
 530 inferred from magnetotelluric data. *Nat. Geosci.* 2, 785–789.
 531 Hirschmann, M.M., 2000. Mantle solidus: Experimental constraints and the effects of peridotite
 532 composition. *Geochemistry, Geophys. Geosystems* 1.
 533 Jackson, I., Faul, U.H., Fitz, G.J.D., Tan, B.H., 2004. Shear wave attenuation and dispersion in
 534 melt-bearing olivine polycrystals: 1. Specimen fabrication and mechanical testing. *J.*
 535 *Geophys. Res. Solid Earth* 109.
 536 Jackson, M.D., Blundy, J., Sparks, R.S.J., 2018. Chemical differentiation, cold storage and
 537 remobilization of magma in the Earth's crust. *Nature* 564, 405–409.
 538 Jaxybulatov, K., Shapiro, N.M., Koulakov, I., Mordret, A., Landès, M., Sens-Schönfelder, C.,
 539 2014. A large magmatic sill complex beneath the Toba caldera. *Science* (80-.). 346, 617–
 540 619.
 541 Karato, S.-I., Spetzler, H.A., 1990. Defect microdynamics in minerals and solid-state
 542 mechanisms of seismic wave attenuation and velocity dispersion in the mantle. *Rev.*
 543 *Geophys.* 28, 399–421.
 544 Koulakov, I., Shapiro, N.M., Sens-Schönfelder, C., Luehr, B.G., Gordeev, E.I., Jakovlev, A.,
 545 Abkadyrov, I., Chebrov, D.V., Bushenkova, N., Droznina, S.Y., 2020. Mantle and crustal
 546 sources of magmatic activity of Klyuchevskoy and surrounding volcanoes in Kamchatka
 547 inferred from earthquake tomography. *J. Geophys. Res. Solid Earth* 125, e2020JB020097.
 548 Lekić, V., Matas, J., Panning, M., Romanowicz, B., 2009. Measurement and implications of
 549 frequency dependence of attenuation. *Earth Planet. Sci. Lett.* 282, 285–293.
 550 Li, L., Weidner, D.J., 2008. Effect of phase transitions on compressional-wave velocities in the
 551 Earth's mantle. *Nature* 454, 984–986. <https://doi.org/10.1038/nature07230>
 552 Mavko, G., 1980. Velocity and attenuation in partially molten rocks. *J. Geophys. Res. Solid*
 553 *Earth* 85, 5173–5189.
 554 Mavko, G., Mukerji, T., Dvorkin, J., 2009. *The rock physics handbook Second Edition.*
 555 Cambridge University Press.
 556 Miller, K.J., Zhu, W., Montési, L., Gaetani, G.A., 2014. Experimental quantification of
 557 permeability of partially molten mantle rock. *Earth Planet. Sci. Lett.* 388, 273–282.
 558 Morris, S.J.S., Jackson, I., 2009. Diffusionally assisted grain-boundary sliding and viscoelasticity
 559 of polycrystals. *J. Mech. Phys. Solids.* <https://doi.org/10.1016/j.jmps.2008.12.006>
 560 Niu, Y., 1997. Mantle Melting and Melt Extraction Processes beneath Ocean Ridges: Evidence
 561 from Abyssal Peridotites. *J. Petrol.* 38, 1047–1074. <https://doi.org/10.1093/petroj/38.8.1047>
 562 O'Connell, R.J., Budiansky, B., 1977. Viscoelastic properties of fluid-saturated cracked solids.
 563 *J. Geophys. Res.* 82, 5719–5735.
 564 Pinel, V., Jaupart, C., Albino, F., 2010. On the relationship between cycles of eruptive activity
 565 and growth of a volcanic edifice. *J. Volcanol. Geotherm. Res.* 194, 150–164.
 566 Prudencio, J., Manga, M., 2020. 3-D seismic attenuation structure of Long Valley caldera:
 567 looking for melt bodies in the shallow crust. *Geophys. J. Int.* 220, 1677–1686.
 568 Reuss, A., 1929. Berechnung der fließgrenze von mischkristallen auf grund der
 569 plastizitätsbedingung für einkristalle. *ZAMM- Journal Appl. Math. Mech. für Angew.*
 570 *Math. und Mech.* 9, 49–58.
 571 Reynolds, O., 1885. LVII. On the dilatancy of media composed of rigid particles in contact. With
 572 experimental illustrations. *London, Edinburgh, Dublin Philos. Mag. J. Sci.* 20, 469–481.

573 Ricard, Y., 2015. 7.02 - Physics of Mantle Convection, in: Schubert, G. (Ed.), . Elsevier, Oxford,
574 pp. 23–71. <https://doi.org/https://doi.org/10.1016/B978-0-444-53802-4.00127-5>

575 Ricard, Y., Matas, J., Chambat, F., 2009. Seismic attenuation in a phase change coexistence
576 loop. *Phys. Earth Planet. Inter.* 176, 124–131.
577 <https://doi.org/https://doi.org/10.1016/j.pepi.2009.04.007>

578 Rychert, C.A., Laske, G., Harmon, N., Shearer, P.M., 2013. Seismic imaging of melt in a
579 displaced Hawaiian plume. *Nat. Geosci.* 6, 657–660.

580 Shapiro, N.M., Droznin, D.V., Droznina, S.Y., Senyukov, S.L., Gusev, A.A., Gordeev, E.I.,
581 2017. Deep and shallow long-period volcanic seismicity linked by fluid-pressure transfer.
582 *Nat. Geosci.* 10, 442–445.

583 Skempton, A.W., 1954. The pore-pressure coefficients A and B. *Geotechnique* 4, 143–147.

584 Sobolev, S.V., Sobolev, A.V., Kuzmin, D.V., Krivolutsкая, N.A., Petrunin, A.G., Arndt, N.T.,
585 Radko, V.A., Vasiliev, Y.R., 2011. Linking mantle plumes, large igneous provinces and
586 environmental catastrophes. *Nature* 477, 312–316.

587 Thybo, H., 2006. The heterogeneous upper mantle low velocity zone. *Tectonophysics* 416, 53–
588 79. <https://doi.org/https://doi.org/10.1016/j.tecto.2005.11.021>

589 Vaišnys, J.R., 1968. Propagation of acoustic waves through a system undergoing phase
590 transformations. *J. Geophys. Res.* 73, 7675–7683.

591 van Hunen, J., Zhong, S., Shapiro, N.M., Ritzwoller, M.H., 2005. New evidence for dislocation
592 creep from 3-D geodynamic modeling of the Pacific upper mantle structure. *Earth Planet.*
593 *Sci. Lett.* 238, 146–155.

594 Voigt, W., 1890. Bestimmung der Elasticitätsconstanten des brasilianischen Turmalines. *Ann.*
595 *Phys.* 277, 712–724. <https://doi.org/10.1002/andp.18902771205>

596 Watanabe, T., Kurita, K., 1993. The relationship between electrical conductivity and melt
597 fraction in a partially molten simple system: Archie’s law behavior. *Phys. earth Planet.*
598 *Inter.* 78, 9–17.

599 Yamauchi, H., Takei, Y., 2016. Polycrystal anelasticity at near-solidus temperatures. *J. Geophys.*
600 *Res. Solid Earth* 121, 7790–7820. <https://doi.org/10.1002/2016JB013316>

601 Zhu, W., Gaetani, G.A., Fosseis, F., Montési, L.G.J., De Carlo, F., 2011. Microtomography of
602 partially molten rocks: three-dimensional melt distribution in mantle peridotite. *Science*
603 (80-.). 332, 88–91. <https://doi.org/10.1126/science.1202221>

604
605

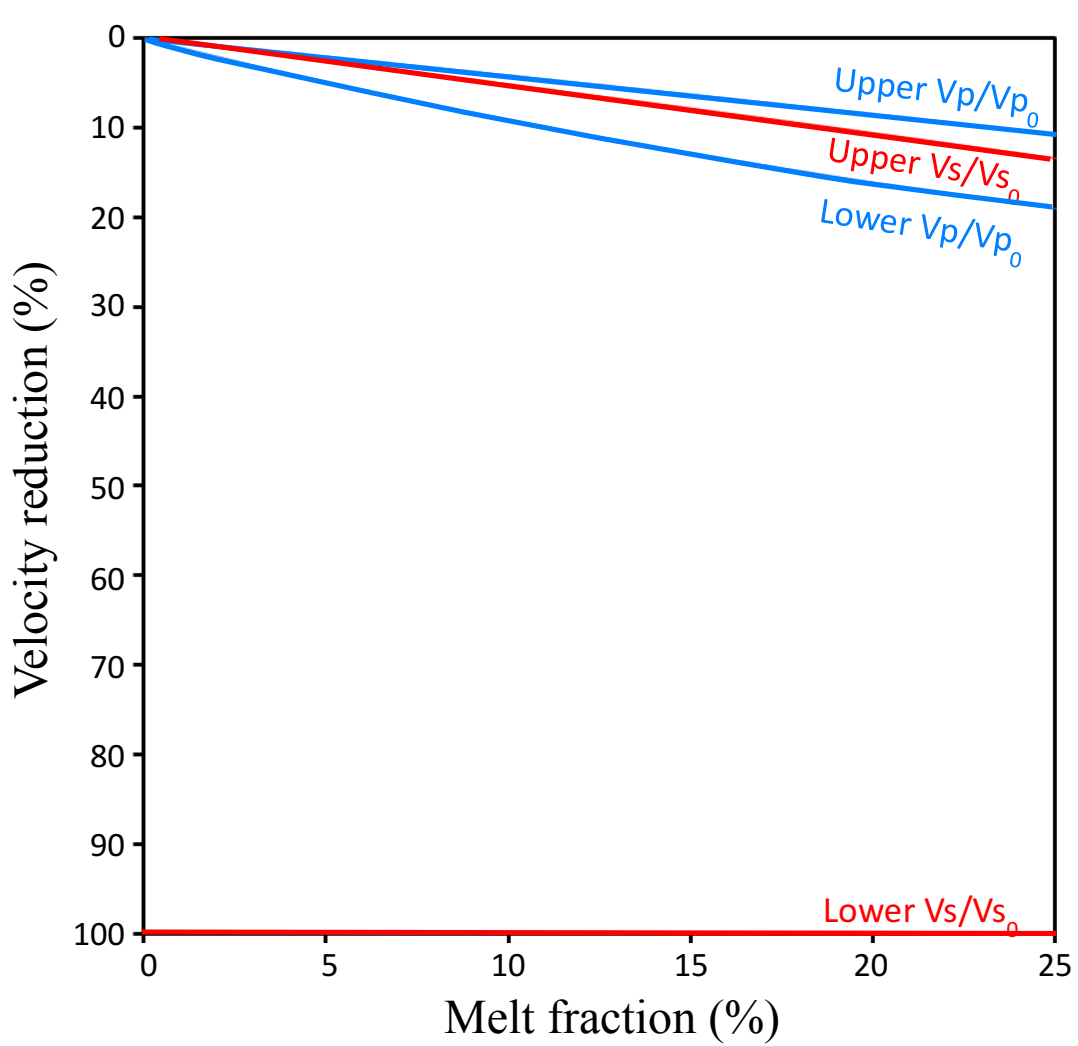
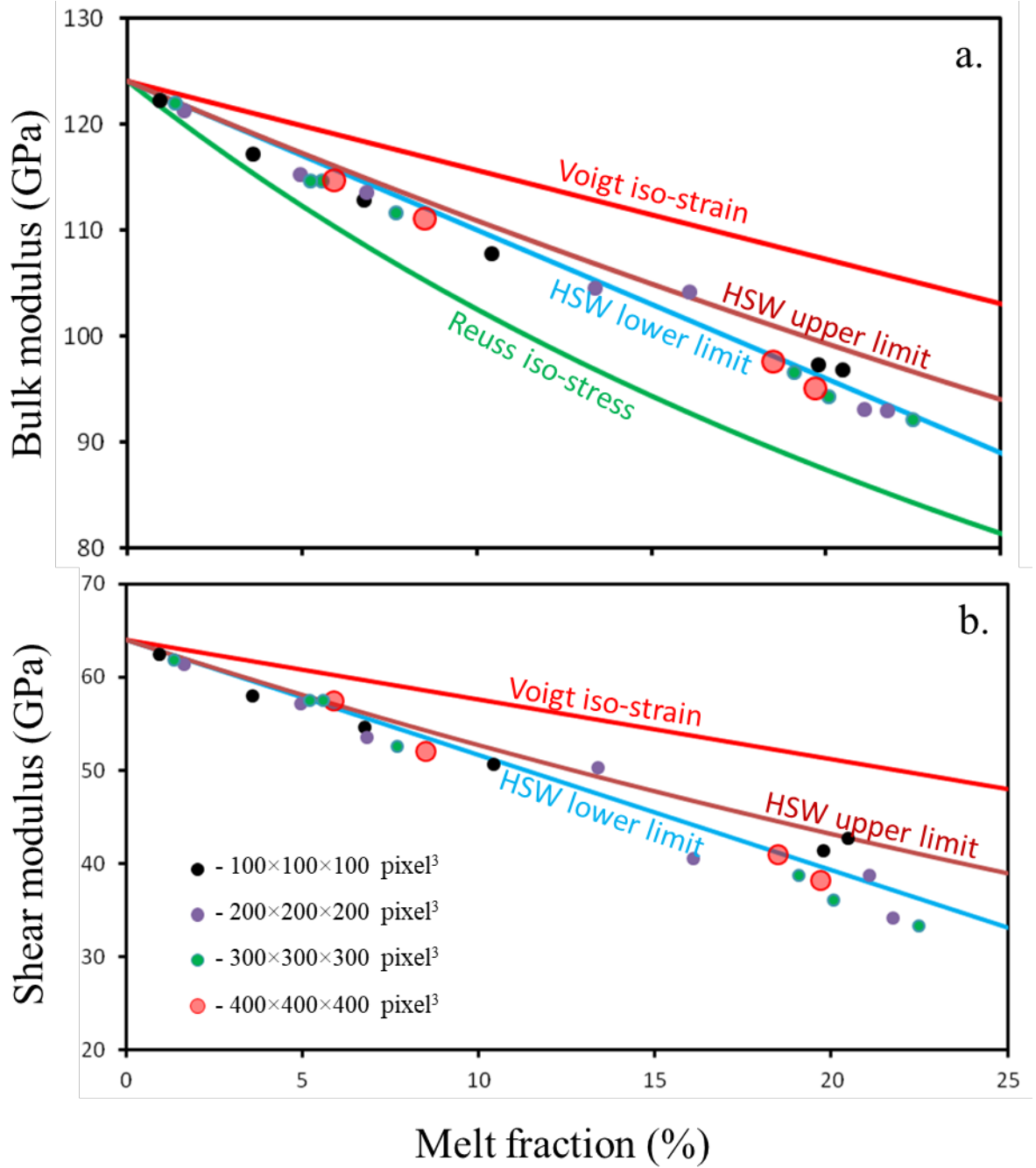


Figure 1: Upper and lower bounds for velocity reduction according to the iso-strain (Upper) and iso-stress (Lower) models, for both, Vp (blue) and Vs (red) seismic velocities.

637
638



639
640
641
642
643

Figure 2: Elastic moduli, bulk (a) and shear (b) for partially molten rock. HSW - Hashin-Shtrikman-Walpole model.

644
645
646
647
648
649
650
651
652
653
654
655
656
657
658
659
660
661
662
663
664
665
666
667
668
669
670
671
672
673
674

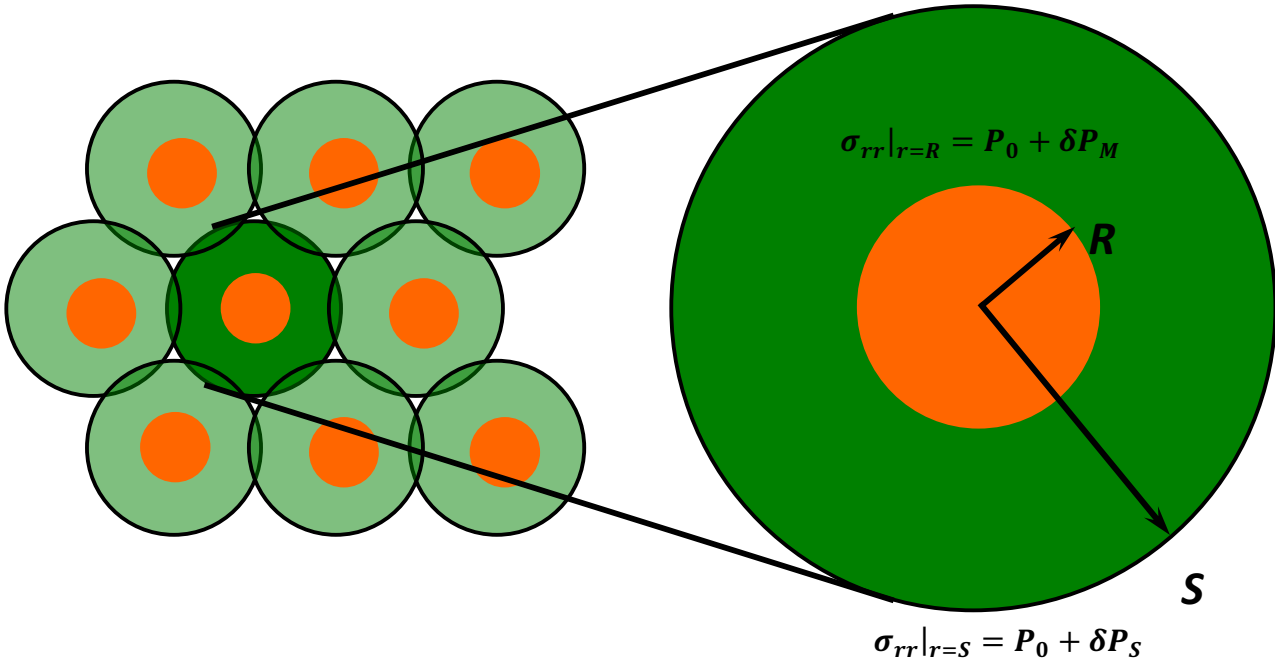


Figure 3: The cell model for spherical melt inclusions in partially melted rocks (see text for further explanation). R and S are the radii of the inclusion and cell, respectively, σ_{rr} is the radial component of the stress in the cell, P_0 is the equilibrium external pressure, under which the melt inclusion co-exists with the surrounding solid shell, and δP_M and δP_S are the pressure oscillations at the inner and outer solid cell boundaries.

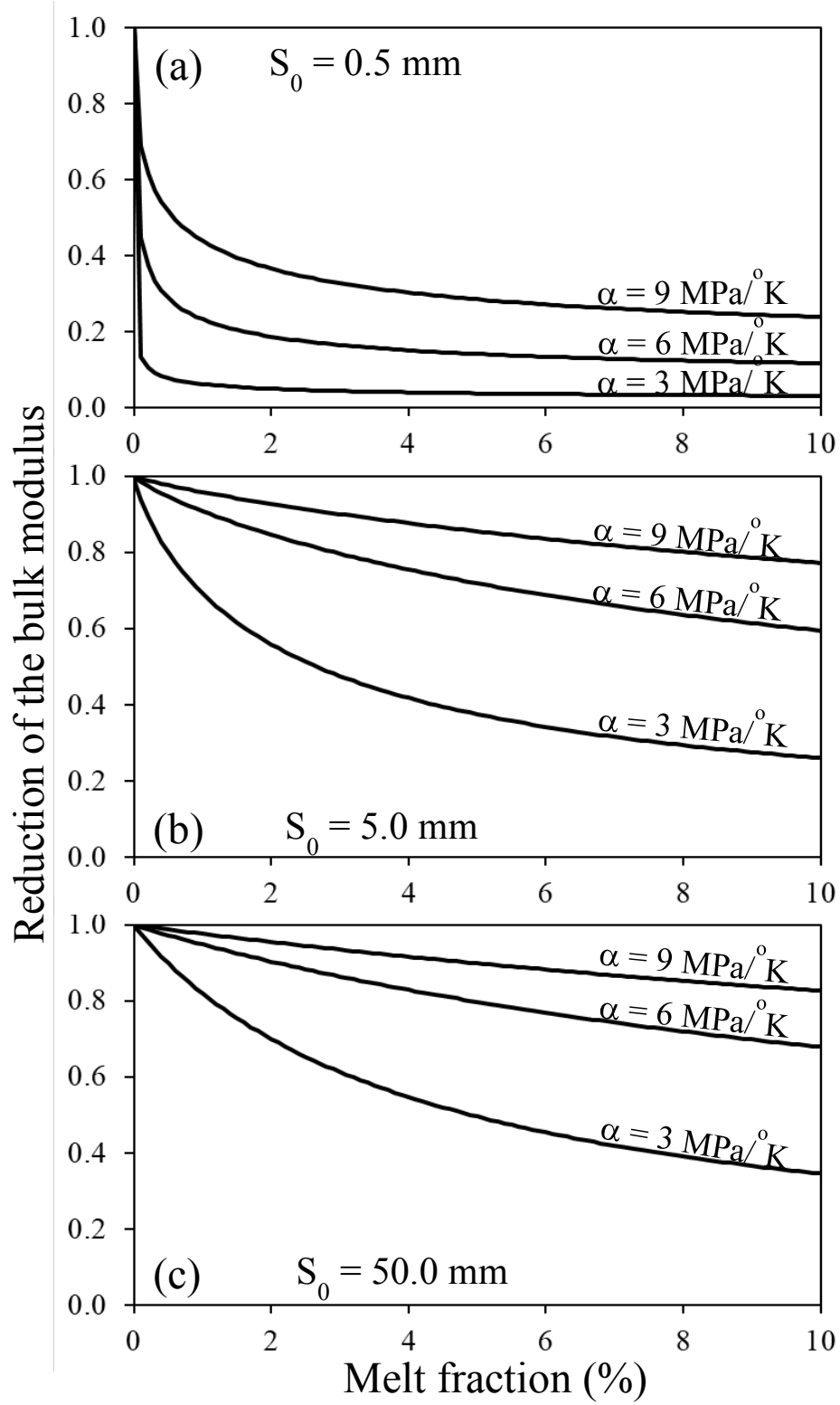
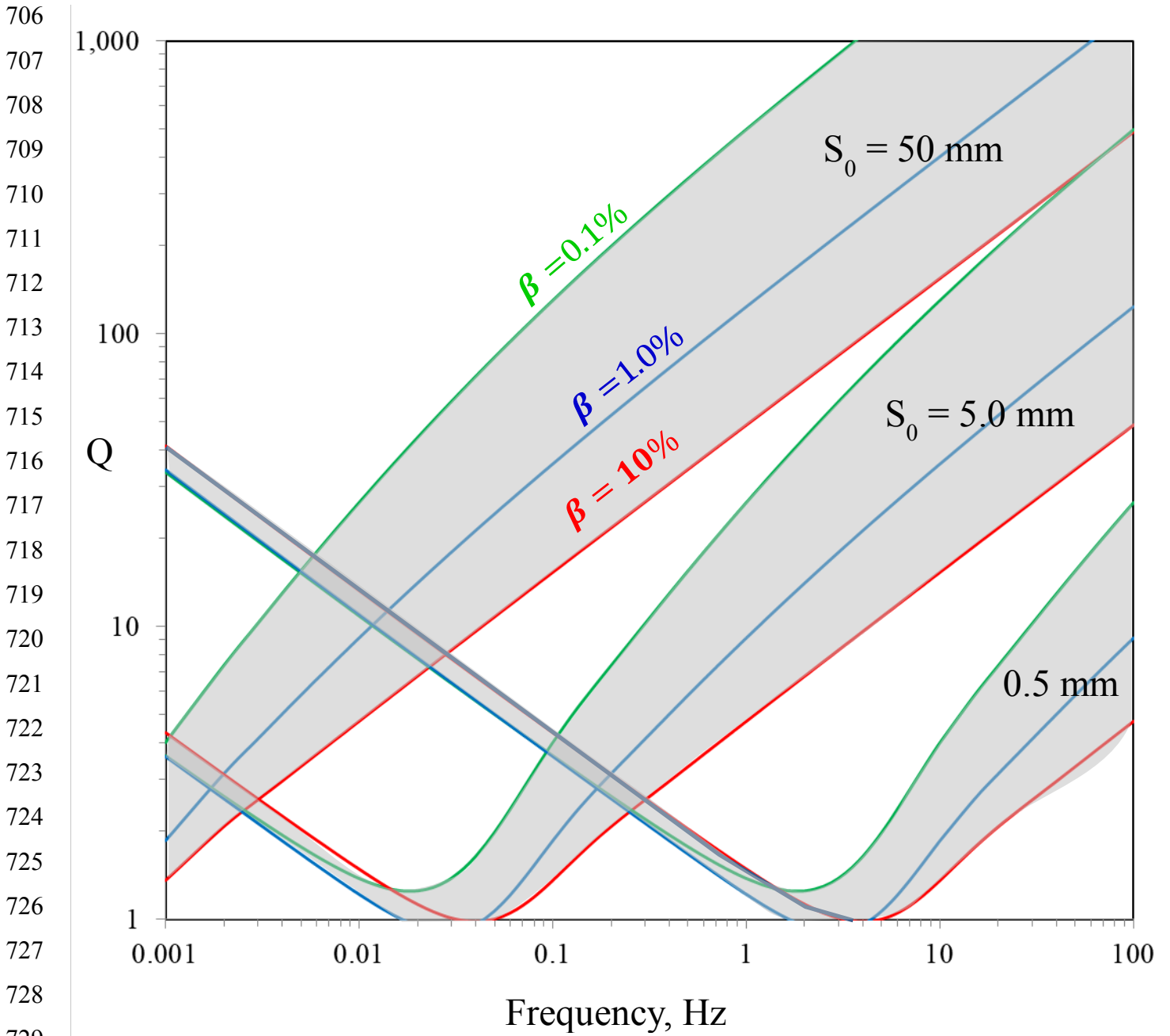


Figure 4: Reduction of the bulk modulus versus melt fraction for different Clausius-Clapeyron slope values $\alpha = 3, 6,$ and $9 \text{ MPa}/^\circ\text{K}$; $S_0 = 0.5 \text{ mm}$ (a), 5.0 mm (b), and 50.0 mm (c), and 1 Hz frequency.



732 **Figure 6:** Q versus frequency for different melt fraction values $b = 0.1\%$, 1.0% , and
 733 10% and Clausius-Clapeyron slope value $a = 5 \text{ MPa}/^\circ\text{K}$. Shaded polygons show Q -values for
 734 $S_0 = 0.5 \text{ mm}$, 5.0 mm , and 50.0 mm .

735
736

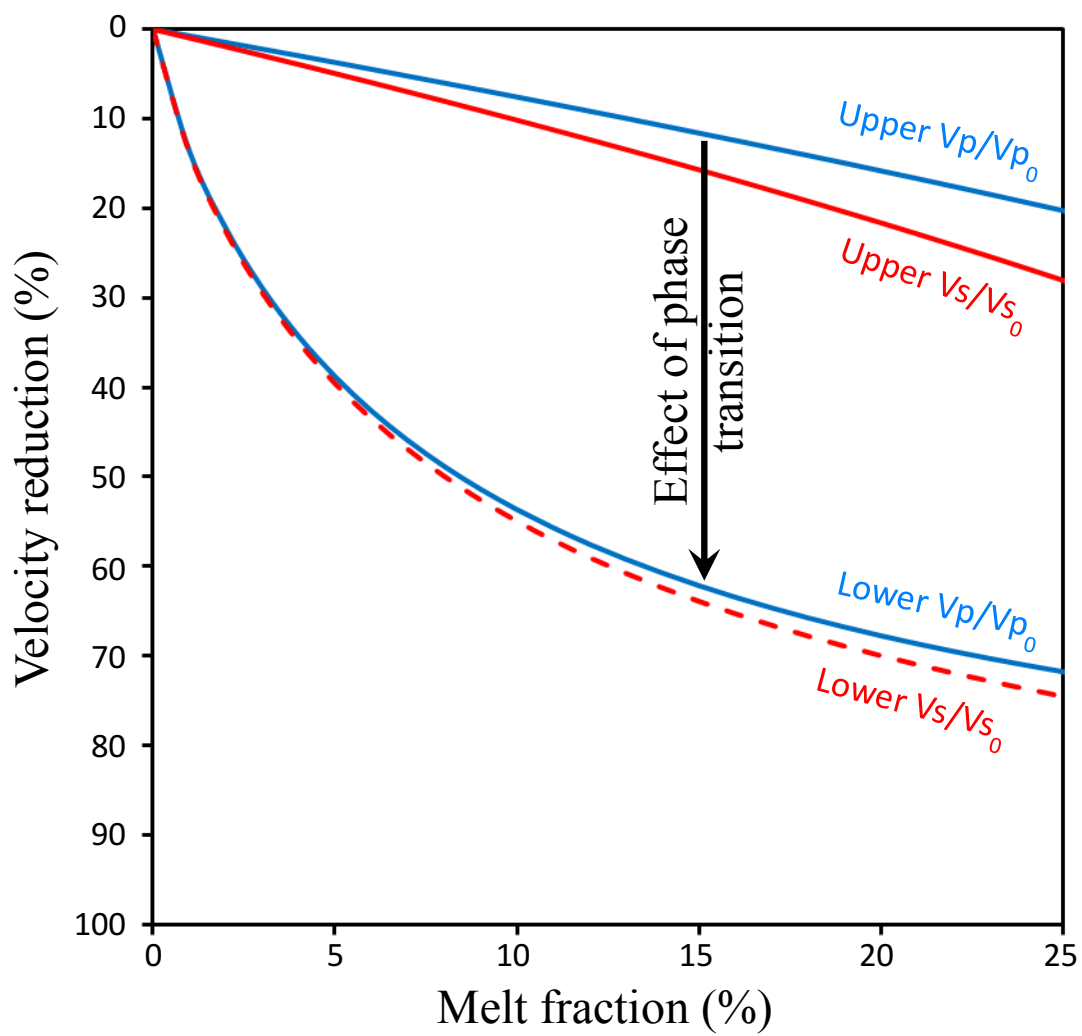


Figure 7: Velocity change predicted by the model with spherical inclusions and corrected after the phase transition effect for $S_0 = 5.0$ mm, $a = 5$ MPa/°K, and 1 Hz frequency.